Sea-ice melting processes inferred from ice–upper ocean relationships in the Ross Sea, Antarctica

Sohey Nihashi,[1,2] Kay I. Ohshima,[3] Martin O. Jeffries,[4] and Toshiyuki Kawamura[3]

Received 5 December 2003; revised 29 October 2004; accepted 15 December 2004; published 5 February 2005.

[1] Sea-ice melting processes are inferred from various summer sea-ice and upper ocean data obtained in the Ross Sea in January 1999. Using spatially (30 km) averaged continuous data, an ice concentration–water temperature plot (CT-plot) shows that the temperature at a depth of ~7 m increases as ice concentration decreases in the ice interior region. The CT-plot is explained by a simple ice–upper ocean coupled model in which sea-ice melting is caused only by heat input through open water. The bulk heat transfer coefficient between ice and ocean (K_b) is estimated to be 1.2×10^{-4} m s^{-1}. These findings are supported by the relationship between ice concentration and heat content in the mixed layer estimated from conductivity-temperature-depth (CTD) data. Salinity at a depth of ~7 m, salt deficit in the mixed layer associated with sea-ice melt estimated from CTD data, and their relationships with ice concentration also suggest that melting is mainly caused by atmospheric heat input through open water and that local balance of salinity nearly hold. The time evolution of ice concentration calculated from the ice–upper ocean coupled model with the estimated K_b corresponds with that derived from the Special Sensor Microwave Imager (SSM/I), confirming the model's applicability and the value of K_b.

Citation: Nihashi, S., K. I. Ohshima, M. O. Jeffries, and T. Kawamura (2005), Sea-ice melting processes inferred from ice–upper ocean relationships in the Ross Sea, Antarctica, *J. Geophys. Res.*, *110*, C02002, doi:10.1029/2003JC002235.

1. Introduction

[2] The Antarctic Ocean has a primarily seasonal sea-ice cover, and most of the ice surface is covered by snow with a high albedo. The fraction of open water is relatively large because of the divergent drift of the ice. The existence of open water with an albedo much lower than sea ice results in high solar radiation absorption in summer [*Maykut and McPhee*, 1995]. This absorption can be the dominant heat source for bottom and lateral melting of the ice [*Maykut and Perovich*, 1987]. These effects become important especially in the marginal and seasonal ice zones.

[3] From a heat budget analysis of the Antarctic Ocean, *Nihashi and Ohshima* [2001] showed that net heat input at the water surface in the active melt season (December–January) is 100–150 W m^{-2} due to large solar heating, and is 1 or 2 orders of magnitude larger than that at the ice surface because of the albedo difference. Further, they showed that heat input into the upper ocean through open water is comparable to the latent heat of sea-ice melting in the entire Antarctic sea-ice zone, and that this heat input is much larger than the estimated heat entrained from the deeper ocean, another possible heat source. *Ackley et al.* [2001] explained the causes for the Ronne polynya observed in the southern Weddell Sea only during austral summer 1997/1998 as follows: The open water fraction was increased by the divergent drift of ice associated with an anomalous wind pattern at the beginning of the melt season, and then large absorption of solar radiation through the open water area sustained the polynya. This mechanism is named the open water–albedo feedback and is supported by a numerical modeling study [*Hunke and Ackley*, 2001]. These studies suggest that heat input into the ice–upper ocean system mainly occurs at open water and its heat then mainly goes into sea-ice decay through bottom and lateral melting. Thus, sea ice and the upper ocean are strongly coupled thermodynamically in the active melt season.

[4] In the Antarctic Ocean, annual variations of the sea-ice cover including the melt season have been examined using various ice-ocean coupled models since the work of *Parkinson and Washington* [1979]. However, there have been very few observational studies that examine the ice–upper ocean coupled system. In the area off Syowa Station (Figure 1), *Ohshima et al.* [1998] measured ice concentration continuously with a video monitoring system aboard the icebreaker *Shirase* along with water temperature and salinity monitoring at a depth of ~8 m toward the end of December 1990. Then they showed characteristic relation-

[1] NASA Goddard Space Flight Center, Greenbelt, Maryland, USA.
[2] Now at Institute of Low Temperature Science, Hokkaido University, Sapporo, Japan.
[3] Institute of Low Temperature Science, Hokkaido University, Sapporo, Japan.
[4] Geophysical Institute, University of Alaska Fairbanks, Fairbanks, Alaska, USA.

0148-0227/05/2003JC002235$09.00

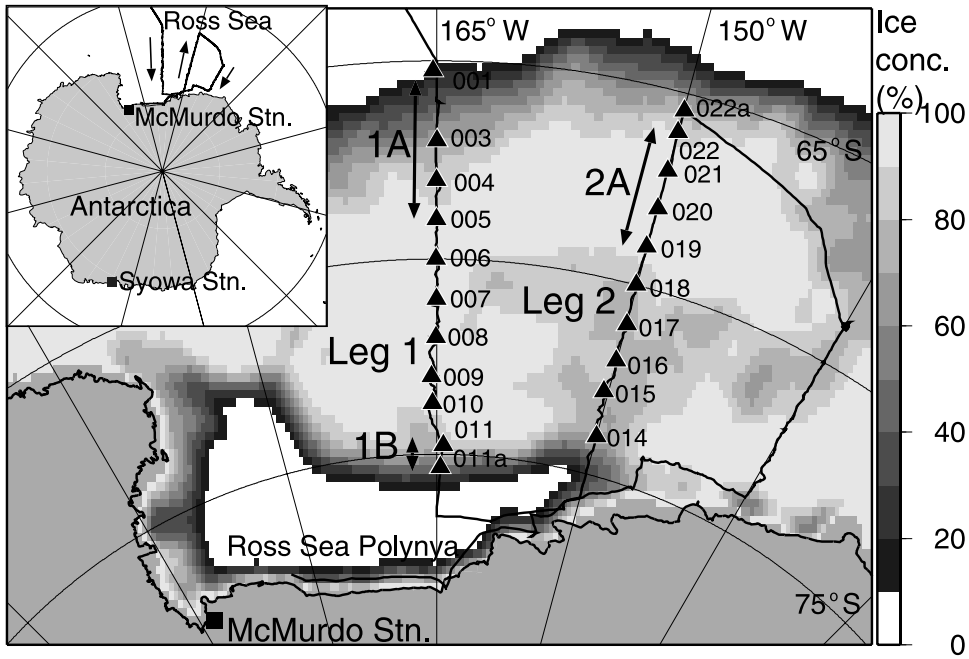

Figure 1. Cruise track of the R/V *Nathaniel B. Palmer* and ice concentration on 1 January 1999 derived from the DMSP SSM/I using the enhanced NASA Team (NT2) algorithm. Triangles indicate CTD stations. The station number corresponds to the Julian day when the observation was made. The locations of Stations 011a and 022a correspond to the ice edges when the observations were made; 1A, 1B, and 2A indicate the analysis areas.

ships among ice concentration, temperature, and salinity in the upper ocean by using spatially averaged data. In the ice interior region, water temperature increased, while salinity decreased as ice concentration decreased. At the ice margin, both temperature and salinity decreased as ice concentration increased. These relationships were explained by an ice–upper ocean coupled model that assumed that sea-ice melting was caused only by heat input through open water.

[5] From the beginning of January 1999, ship-based observations of the sea-ice cover and the upper ocean were made aboard the R/V *Nathaniel B. Palmer* in the Ross Sea (Figure 1). Conditions in the area off Syowa Station and the Ross Sea are similar because both sets of observations were made during the season with nearly maximum heat input and rapid sea-ice retreat. Ice concentration was measured continuously by a video monitoring system. At the same time, water temperature and salinity at a depth of ~7 m were recorded by an underway sampling system. In addition to these measurements, as in the case of the previous study [*Ohshima et al.*, 1998], visual sea-ice observations and conductivity-temperature-depth (CTD) measurements were made during our cruise. The visual observations provide detailed information on sea-ice conditions during the melt season. The CTD data allow us to evaluate the changes in heat content and salinity of the ocean mixed layer associated with ice melt. Further, snow and ice core measurements were made on ice floes [*Morris and Jeffries*, 2001; *Kawamura et al.*, 2005]. These in situ data along with the sea-ice data from a satellite passive microwave radiometer make it possible to infer ice melt processes. The purpose of this paper is to describe sea-ice melting processes taking advantage of various sea-ice and upper ocean data in the summer Ross Sea, also making comparison to the results of a simple ice–upper ocean coupled model.

[6] The paper is organized as follows: The study area, measurements, and data are described in section 2. Section 3 describes ice, ocean, and heat flux conditions. From the data and a simple ice–upper ocean coupled model, we examine the relationships among ice concentration, temperature, and salinity in section 4. Section 5 summarizes the findings.

2. Study Area, Measurements, and Data

[7] In January 1999, the R/V *Nathaniel B. Palmer* operated in the Ross Sea pack ice supporting sea-ice and ocean studies. Figure 1 shows the cruise track. The ship operated along 165°W southward toward the continent during 1 to 11 January. In this study we call this observation line Leg 1. During 14 to 22 January, ice and ocean observations were made along 150°W from near the continent to the ice edge. We call this line Leg 2. Finally, the ship operated along 135°W. This leg is not considered here.

[8] For continuous recording of ice concentration, a forward-looking video camera was installed on the ice tower of the R/V *Nathaniel B. Palmer* at a height of ~25 m from the sea surface. The pixel data of the recorded image are divided into two categories, ice and water, using a suitable gray level threshold. Then, ice concentration was measured along a horizontal row of pixels equivalent to a width of ~100 m every second. We also use daily ice concentration data derived from the Special Sensor Microwave Imager (SSM/I) on the Defense Meteorological Satellite Program (DMSP) F13. The grid resolution is ~25 km. For the calculation of ice concentration, the enhanced NASA Team (NT2) algorithm [*Markus and Cavalieri*, 2000] is used. The results

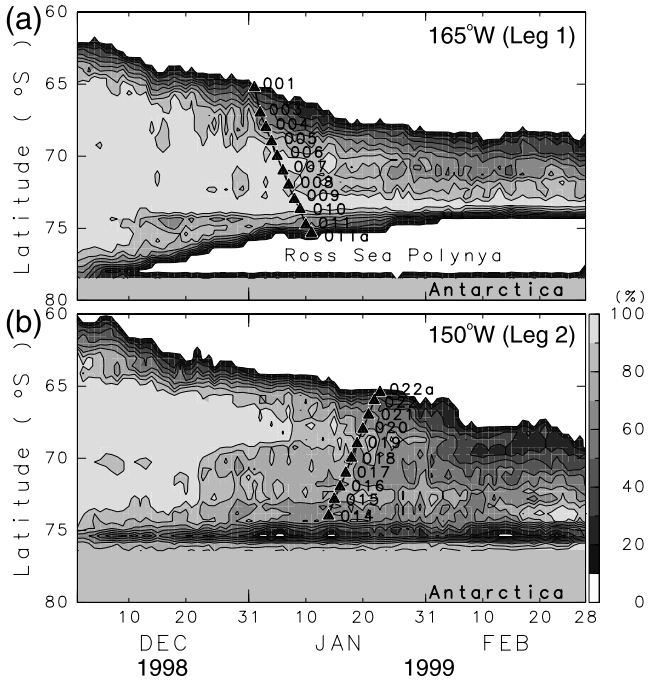

Figure 2. Time series of ice concentration along (a) 165°W (Leg 1) and (b) 150°W (Leg 2), derived from the DMSP SSM/I. The solid lines indicate the latitude of the ship position corresponding to the cruise track (Figure 1), and the triangles indicate the CTD stations.

are compared with ice concentration obtained using the Bootstrap algorithm [*Comiso*, 1995] in Appendix A.

[9] Hourly visual observations of the sea-ice cover were made according to *Worby and Allison* [1999] from the ship's bridge while the ship was underway in the pack ice. For each visual observation the sea-ice cover was divided into three thickness categories, and for each category the concentration, ice type, mean ice thickness, floe size, topography, snow type, and mean snow depth on unridged ice were estimated. In this study, the ice concentration, floe size, and thickness data are used.

[10] The temperature and salinity in the upper ocean were recorded every minute at a depth of ~7 m by the underway sampling system aboard the R/V *Nathaniel B. Palmer*. CTD measurements were made almost every day at ~1° latitude intervals (Figure 1).

[11] For air temperature at 2 m, dew point temperature at 2 m, wind at 10 m, and surface sea level pressure, we use the European Centre for the Medium-Range Weather Forecasts (ECMWF) data with a resolution of 2.5° × 2.5°. Since the data are available twice a day, at 0000 UT and 1200 UT, we averaged them to obtain daily values. For cloud cover, we use International Satellite Cloud Climatology Project (ISCCP) D2 data with a resolution of 2.5° × 2.5°. We averaged the monthly cloud cover from 1983 to 2001 to obtain a climatological data. These data are used for the heat budget calculations in section 3.

3. Ice, Ocean, and Heat Flux Conditions

[12] The Ross Sea polynya is a feature of the Ross Sea. The wide area of open water (Figure 1) appears every summer on the western Ross Sea continental shelf adjacent to the Ross Ice Shelf [*Gloersen et al.*, 1992]. From data analysis and modeling, it has been suggested that both divergent drift of ice by the wind and the inflow of relatively warm Circumpolar Deep Water (CDW) onto the continental shelf are essential for the formation of this polynya [*Jacobs and Comiso*, 1989; *Fichefet and Goosse*, 1999].

[13] Figures 2a and 2b show the time series of ice concentration during austral summer 1998/1999 along 165°W and 150°W corresponding to Leg 1 and Leg 2, respectively. Along 165°W, the ice edge retreated rapidly between early December and the middle of January. The Ross Sea polynya began to appear in the middle of December. Although the polynya area enlarged rapidly in December, it did not change much after the beginning of January when the observations were being made from the ship. Along 150°W, ice concentration decreased in December and the ice edge retreated rapidly. However, the changes in ice concentration and position of the ice edge were small during the period of ship-based observations. Satellite and in situ observations have shown that a perennial ice zone exists in the eastern Ross Sea almost every year [*Gloersen et al.*, 1992; *Jeffries et al.*, 1994]. According to SSM/I data, sea ice survived during summer of 1998/1999 along both Leg 1 and Leg 2 (Figures 2a and 2b). In the vicinity of the area between 73°S and 74°S along Leg 1, high ice concentrations (≥90%) persisted until the end of February (Figure 2a).

[14] Some vertical CTD profiles are shown in Figure 3. In almost all areas, stratification of the upper ocean (≤30 m) was well developed because the temperature was raised by solar heating and the salinity was reduced by sea-ice melting. From these vertical profiles, it is expected that the temperature and salinity monitored by the underway sampling system at a depth of ~7 m approximately represent the values averaged over the surface mixed layer. The water temperature recorded by the underway sampling system was only ~0.02°C higher than that at the same depth by the CTD. Raw temperature and salinity monitored by the underway sampling system are used in this study.

[15] Figures 4a–4d and 5a–5d show the distribution of the observed ice and ocean characteristics along the cruise tracks of Leg 1 and Leg 2, respectively. Ice thicknesses at the area in which high ice concentration persisted (between Stations 009 and 010; Figure 2a) and the surrounding area along Leg 1 were ~4 m, and were significantly different from that of other areas along the cruise track (≤1 m; Figures 4a and 5a).

[16] Table 1 shows average net heat input at the water and ice surfaces for a month before the observation calculated at the grid points of the ECMWF data nearest the cruise tracks of Leg 1 and Leg 2. Heat fluxes are calculated based on the bulk and empirical formulae used by *Nihashi and Ohshima* [2001]. Specifically, the empirical formulae for the incoming shortwave radiation and the incoming longwave radiation are calculated according to *Zillman* [1972] and *König-Lango and Augstein* [1994], respectively. Each component of heat flux calculated using these formulae is comparable to that derived from in situ data in summer [*Launiainen and Vihma*, 1994]. Atmospheric input data obtained aboard the R/V *Nathaniel B. Palmer* are similar

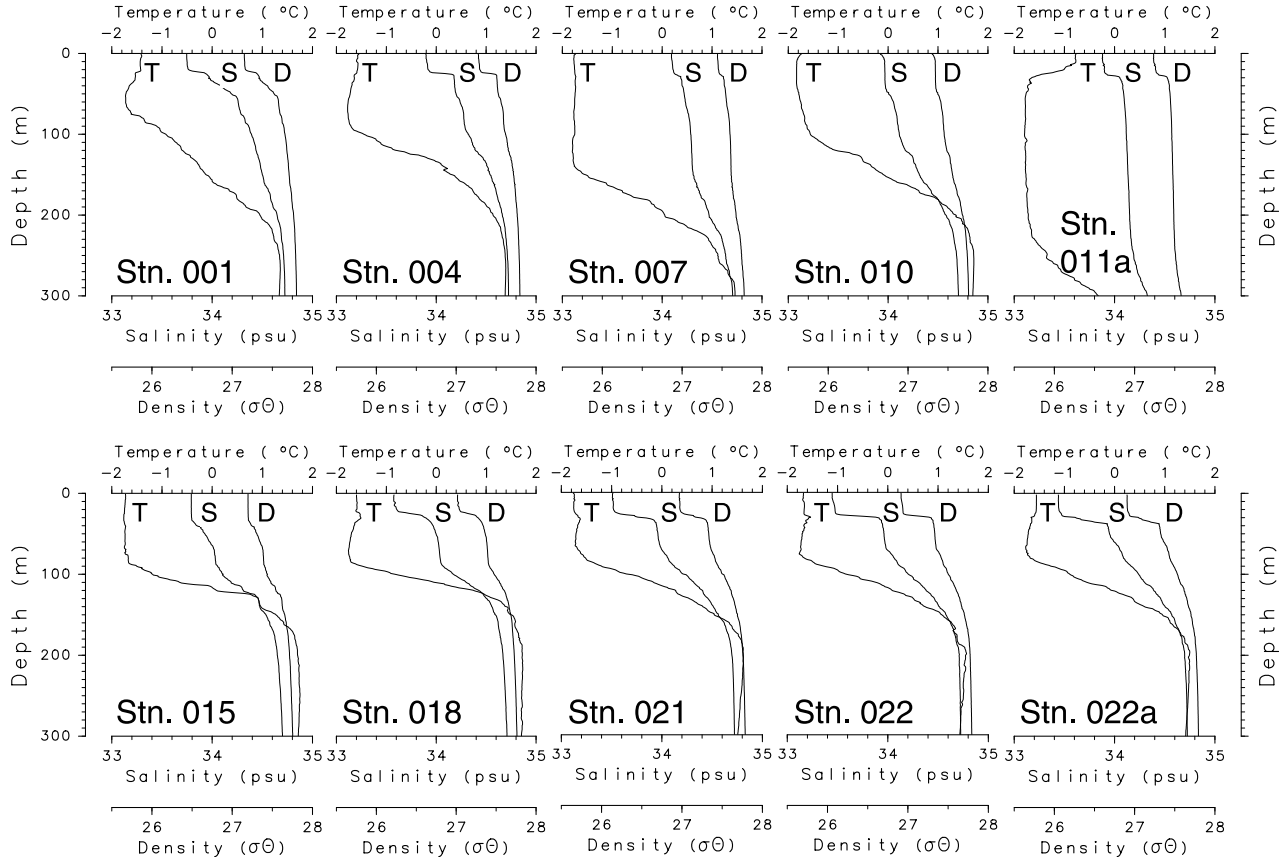

Figure 3. Vertical profiles of water temperature (T), salinity (S), and potential density (D) obtained by CTD. Locations of the stations are indicated in Figure 1.

to the corresponding ECMWF data. Calculating the net heat input at the water and ice surfaces using the in situ and ECMWF data yields differences of only 5 W m^{-2} and 1 W m^{-2}, respectively. In order to calculate heat fluxes for a longer period, we use the ECMWF data for input data. From Table 1, the net heat input at the water surface is ~150 W m^{-2}, while that at the ice surface is close to 0 W m^{-2}, suggesting that heat input mainly occurs at the open water area. Although there was evidence for snow melting and refreezing [*Morris and Jeffries*, 2001; *Kawamura et al.*, 2005], from the video and visual observations, there were no melt ponds on the ice surface, as are observed throughout the summer Arctic sea-ice cover.

4. Relationships Among Ice Concentration, Temperature, and Salinity

[17] Relationships between ice concentration derived from the video system and the upper ocean monitored by the underway sampling system are examined in regions 1A, 1B, and 2A (Figure 1). In these regions, ice concentration data derived from the video system, visual observations, and SSM/I correspond with each other relatively well; thus the reliability of the video data is expected to be high (see Appendix B). Region 1A, the area between Stations 001 and 005 along Leg 1, corresponds to a pack ice region ~50 km south of the ice edge. Region 1B, the area between Station 011 and the southern ice edge along Leg 1, corresponds to an ice margin region adjacent to the Ross Sea polynya. Region 2A, the area between Stations 019 and 022 along Leg 2, corresponds to a pack ice region away from the ice-free ocean, polynya, and coast. For consistency with the previous study [*Ohshima et al.*, 1998], we call regions 1A and 2A "ice interior region."

4.1. Relationship Between Ice Concentration and Temperature

[18] Figures 6a, 6b, and 6c show ice concentration–temperature plots (hereinafter CT-plot) for regions 1A, 1B, and 2A, respectively. Water temperature increases as ice concentration decreases both in the ice interior region (1A) and at the ice margin adjacent to the Ross Sea polynya (1B) (Figures 6a and 6b), consistent with results obtained for the area off Syowa Station [*Ohshima et al.*, 1998]. In the Syowa Station area, the correlation coefficients among ice concentration, temperature, and salinity in the upper ocean increased, particularly when 20–30 km running mean data were used, suggesting that local balances of heat and salinity in the ice–upper ocean system approximately hold over that spatial scale, while the effects of ice advection are dominant at smaller scales. A similar result is found in the summer Ross Sea by using ice concentration data derived from the video system and upper ocean data monitored by the underway sampling system. The correlation coefficient between ice concentration and temperature increases (~0.7) particularly around the running mean distance of 15–30 km. It is low (≤0.4) for the raw data. Therefore 15–30 km running mean data along the cruise track are used

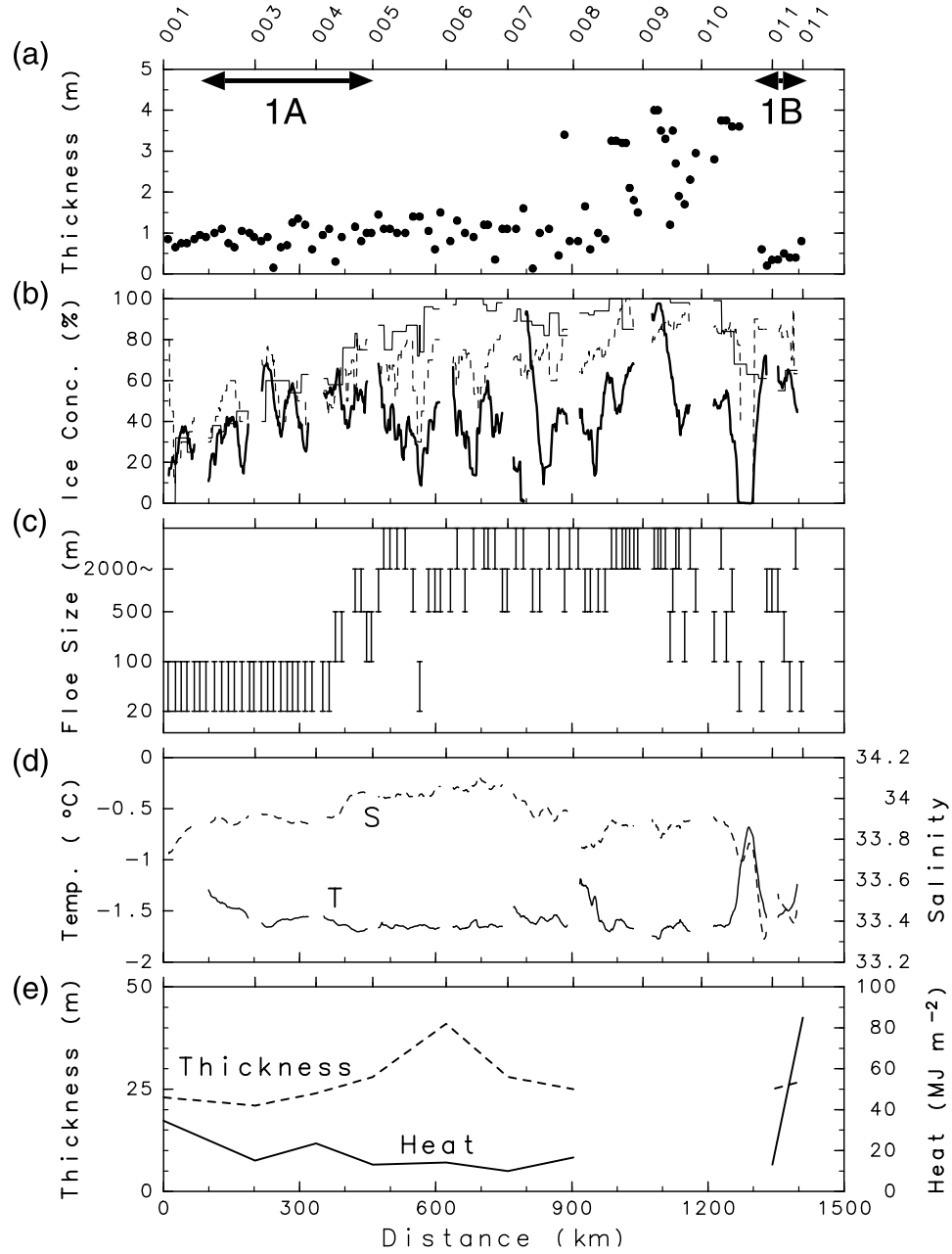

Figure 4. Distribution of sea-ice and upper ocean characteristics along Leg 1. (a) Ice thickness obtained by visual observation. (b) Ice concentration derived from the video monitoring system (thick solid line), visual observation (thin dashed line), and SSM/I (thin solid line). The video and visual data have been smoothed using a 25 km running mean. (c) Ice floe size obtained by visual observation. (d) Water temperature (solid line) and salinity (dotted line) at a depth of ~7 m from the underway sampling system smoothed using a 25-km running mean. Sea ice and T, S data (Figures 4a–4d) are drawn when the ship was underway in the pack ice. (e) Thickness (dotted line) and heat content (solid line) of the surface mixed layer estimated from the CTD data (Figure 3). The data at Stations 009 and 010 are not shown because the mixed layer cannot be identified. In Figure 4a, CTD stations (Figure 1) are indicated along the top and 1A and 1B indicate the analysis areas (Figure 1). In Figure 4e, the distance from the ice edge in the north to the continent in the south is indicated along the bottom.

in this study. The CT-plot for region 2A (Figure 6c) does not show the characteristic relationship, probably because the water temperature range is small over a broad area.

[19] Since heat input into the ice–upper ocean system mainly occurs at open water (Table 1), we examine the observed CT-plot using a simple ice–upper ocean coupled model in which sea-ice melting is caused only by heat input through open water (proposed by *Ohshima and Nihashi* [2005]). Here we briefly describe the model, shown schematically in Figure 7. One oceanic surface mixed layer is

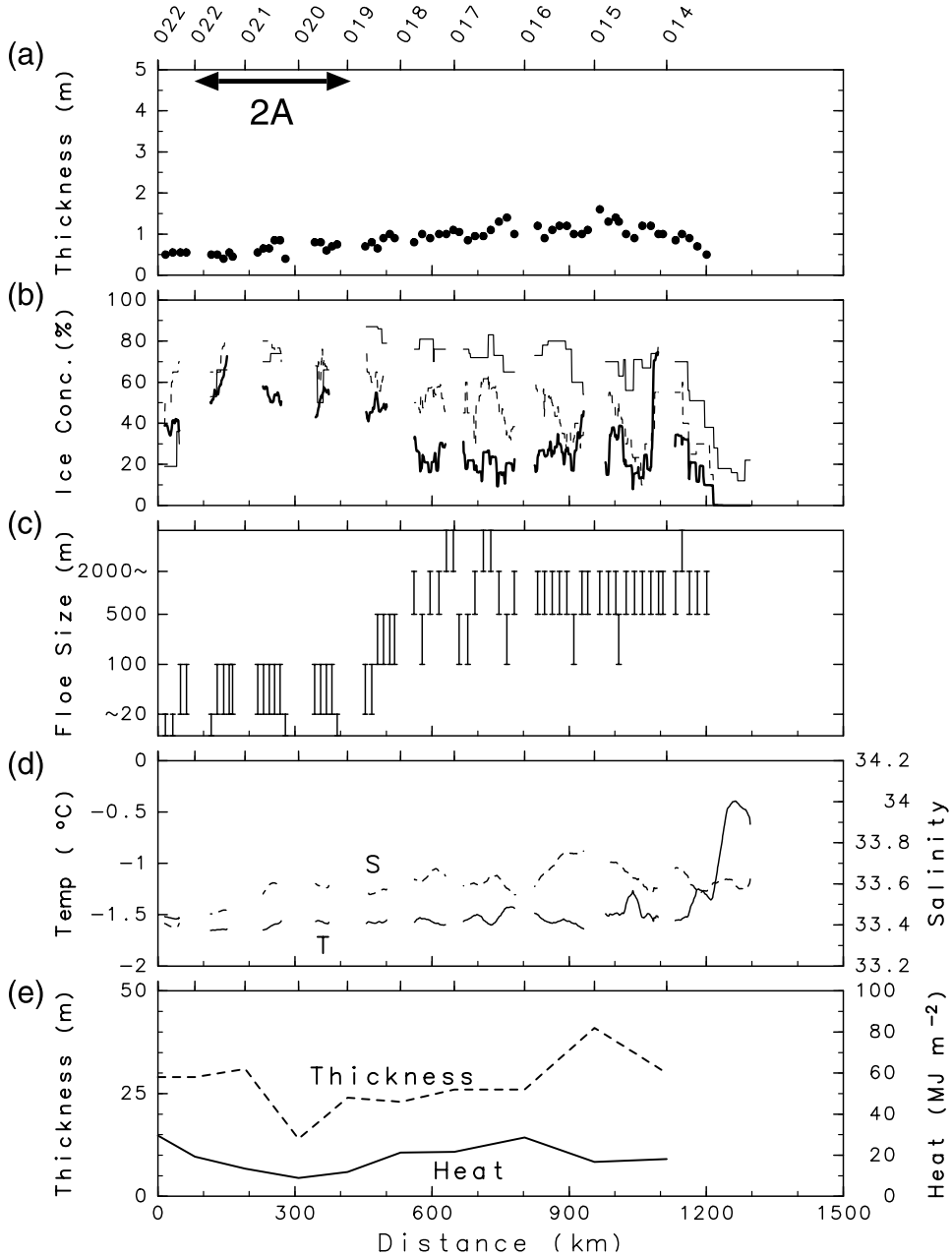

Figure 5. As in Figure 4, except for Leg 2.

assumed with constant thickness (H). The ice thickness h_0 is defined as the average thickness of individual floes comprising the ice medium and assumed to be constant. Sea-ice melting is represented only by a decrease in ice concentration (C). Heat input into the ice–upper ocean system is represented as the product of net heat input at the water surface (F_n) and the open water fraction ($1 - C$). If sea-ice melting is caused by this heat input, the heat balance of the upper ocean is given by

$$c_w \rho_w H \frac{dT}{dt} = F_n(1 - C) + L_f \rho_i h_0 \frac{dC}{dt}, \tag{1}$$

where c_w(= 3990 J kg^{-1} °C^{-1}) is the heat capacity of seawater; ρ_w(= 1026 kg m^{-3}) and ρ_i(= 900 kg m^{-3}) are the densities of seawater and sea ice, respectively; L_f is the latent heat of fusion for sea ice; and t is time. A fixed value of L_f = 0.276 MJ kg^{-1} corresponding to an observed ice salinity of 6 practical salinity unit (psu) is used. The melting rate of sea ice ($-L_f \rho_i h_0 \frac{dC}{dt}$) is assumed to be proportional to the difference between water temperature (T) and the freezing point (T_f = −1.86°C) and is parameterized as follows:

$$-L_f \rho_i h_0 \frac{dC}{dt} = c_w \rho_w K_b C(T - T_f), \tag{2}$$

where K_b is the bulk heat transfer coefficient between ice and ocean.

Table 1. Average Net Heat Input at the Water Surface and at the Ice Surface for a Month Before the Observations[a]

Location	Water Surface	Ice Surface
65.0°S–75.0°S, 165°W (Leg 1)	155	1
65.0°S–75.0°S, 150°W (Leg 2)	151	1
67.5°S, 165°W (1A)	158	0
75°S, 165°W (1B)	151	0
67.5°S, 150°W (2A)	146	1

[a]Net heat input is calculated at the grid points of the ECMWF data. The water surface temperature is set to −1.5°C, based on in situ observation. Values are in W m^{-2}.

[20] Time evolutions of ice concentration (C) and water temperature (T) calculated from the ice–upper ocean coupled model (equations (1) and (2)) show that they converge asymptotically to a single curve with a timescale of ∼10 days regardless of initial conditions (Figure 8). The convergent curve obtained from the model by giving realistic parameters is compared with the observed CT-plot for region 1A (Figure 6a). Region 1A is chosen because it is an ice interior region away from the ice-free ocean and thus the ice–upper ocean interaction is expected to be approximately in an equilibrium state of local balance. Further, a wide range of observed ice concentration data is necessary to determine K_b value from a comparison with the model result, as will be described later. In regions 1B and 2A, the data amount and range are too small (Figures 6b and 6c) to compare with model results. In the model, the upper ocean is taken as the summer surface mixed layer. Figures 4e and 5e show the thickness of the surface layer estimated from the vertical profile of potential density obtained by CTD (Figure 3). The surface layer thickness is nearly uniform (∼25 m) for region 1A; thus we use a constant value of 25 m as the thickness of the mixed layer (H). From the visual observations of ice thickness, the mean ice thickness (h_0) is set to 0.65 m. F_n is set to 160 W m^{-2} (Table 1).

[21] Figure 9a shows the convergent curve for region 1A superimposed on the observed CT-plot (Figure 6a), where the bulk heat transfer coefficient ($K_b = 1.2 \times 10^{-4}$ m s^{-1}) is determined by least squares fitting to the CT-plot. The observed CT-plot can be well explained by the model. A CT-plot for region 1A using ice concentration derived from the SSM/I with wider viewing range than the ship-mounted video (Appendix B) is superimposed on Figure 9a. Although the range of ice concentration is a little different, similar features are obtained. The CT-plot using the SSM/I data is also distributed near the convergent curve with the same K_b (1.2×10^{-4} m s^{-1}). The fact that similar CT-plots

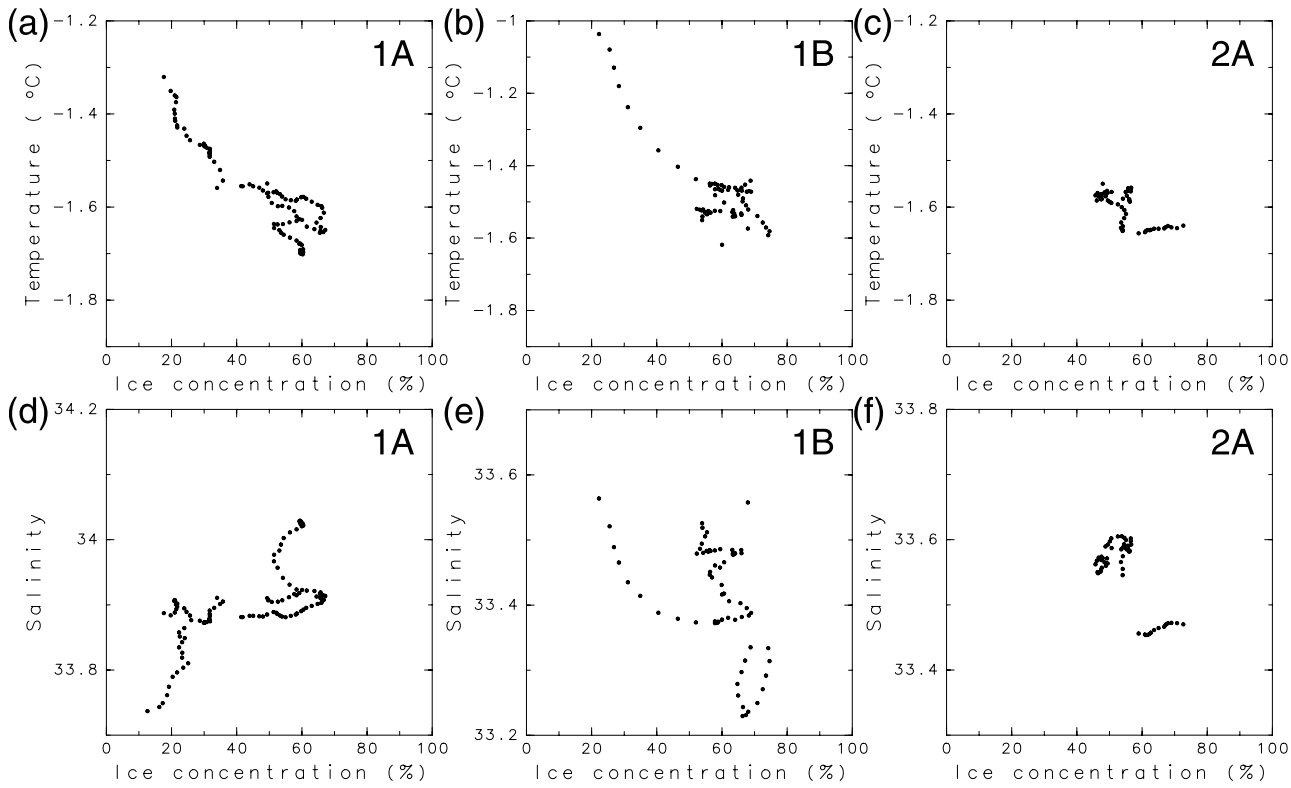

Figure 6. Scatterplots of (a–c) ice concentration versus water temperature and (d–f) ice concentration versus salinity for the running mean data. The ice concentration data are derived from the video system, and the upper ocean data are taken with the underway sampling system. Figures 6a and 6d show results for region 1A, corresponding to the ice interior region, where we use 30-km running mean data. Figures 6b and 6e show results for region 1B, corresponding to the ice margin of the Ross Sea polynya, where we use 15-km running mean data. Figures 6c and 6f show results for region 2A, corresponding to the ice interior region, where we use 30-km running mean data.

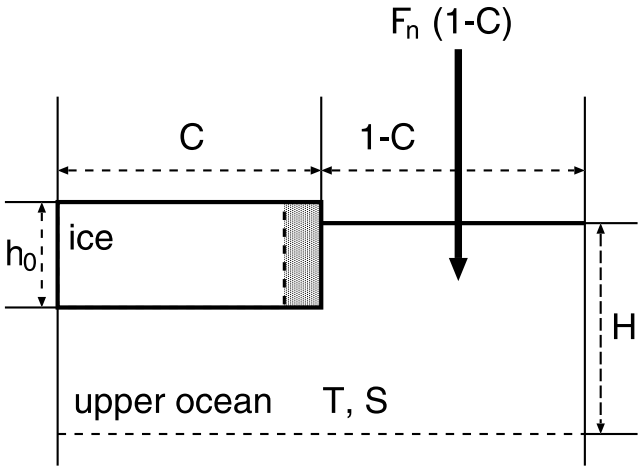

Figure 7. A schematic illustration of the ice–upper ocean coupled model. C is ice concentration; thus 1-C is the open water fraction. For convenience, all the ice is shown as one piece of average thickness h_0, where h_0 is assumed to be constant; thus the ice melting is represented by a decrease in C. The upper ocean is simply represented by one layer of thickness H with uniform temperature T and salinity S. F_n is net heat input at the water surface. Heat input into the ice–upper ocean system occurs only at the open water area.

are obtained is partly because the resolution of the SSM/I data (~25 km) corresponds to the running mean distance of 30 km for the video data.

[22] From observations made at the bottom of sea ice in the Arctic marginal ice zones (the summer Greenland Sea, the late autumn eastern Arctic pack ice, and north of the winter Fram Strait), using the eddy mean correlation method, K_b can be estimated to be $0.5 \times 10^{-4} - 0.6 \times 10^{-4}$ m s^{-1} assuming a typical friction velocity (u_{*0}) of 0.01 m s^{-1} [*McPhee*, 1992]. In the autumn Weddell Sea, Antarctica, K_b can be estimated to be $\sim 0.6 \times 10^{-4}$ m s^{-1} from observation at the ice bottom [*McPhee and Martinson*, 1994]. The value in our case ($K_b = 1.2 \times 10^{-4}$ m s^{-1}) is twice as large as those above. This may be reasonable because the heat transfer coefficient in the model is a bulk coefficient which includes lateral melting and melting through brash ice in addition to bottom melting. A similar K_b value ($\simeq 1.2 \times 10^{-4}$ m s^{-1}) was obtained from CT-plot analysis in the area off Syowa Station [*Ohshima and Nihashi*, 2005]. Thus a K_b value of 1.2×10^{-4} m s^{-1} may be typical for the Antarctic sea-ice melt season.

[23] The ice–upper ocean coupled model defined by equations (1) and (2) can also describe the time evolution of ice concentration; for January 1999 this is calculated using the same input parameters (H = 25 m, h_0 = 0.65 m, and $K_b = 1.2 \times 10^{-4}$ m s^{-1}) as those used to calculate the convergent curve for region 1A (Figure 9a). From the monthly averaged value in January, F_n is set to 140 W m^{-2}. For simplification, the values of these input parameters are constant during the calculation. The initial water temperature is set to −1.6°C (Figure 6a). The initial ice concentration is obtained from SSM/I. The calculated time evolution of ice concentration for region 1A corresponds to that derived from the SSM/I (Figure 10). The average difference of ice concentration between the model and observation is −3.9% with standard deviation of 4.4%. Both the CT-plot and the time evolution of ice concentration can be roughly explained by the same model with the same K_b. This supports the applicability of the model and the value of K_b.

[24] In the above discussions we assumed that the temperature (T) observed by the underway sampling system at a depth of ~7 m represents the temperature of the surface mixed layer with constant thickness. The heat content of the mixed layer (Q_u) is a more meaningful quantity that represents the thermodynamic state. It can be estimated from the CTD data. Here Q_u is defined as the energy required to warm the mixed layer from the freezing point (T_f) to a temperature $T(z)$ observed at a depth z in the water column, and is given by

$$Q_u = \int_{z=-H}^{z=0} \rho_w c_w \big(T(z) - T_f\big) dz, \tag{3}$$

where H is the estimated thickness of the mixed layer (Figures 4e and 5e). The estimated Q_u along Leg 1 and Leg 2 is shown in Figures 4e and 5e, respectively.

[25] Figure 11 shows an ice concentration–heat content plot (hereinafter CQ-plot) for Leg 1, including regions 1A and 1B. Since video measurements were not made at the

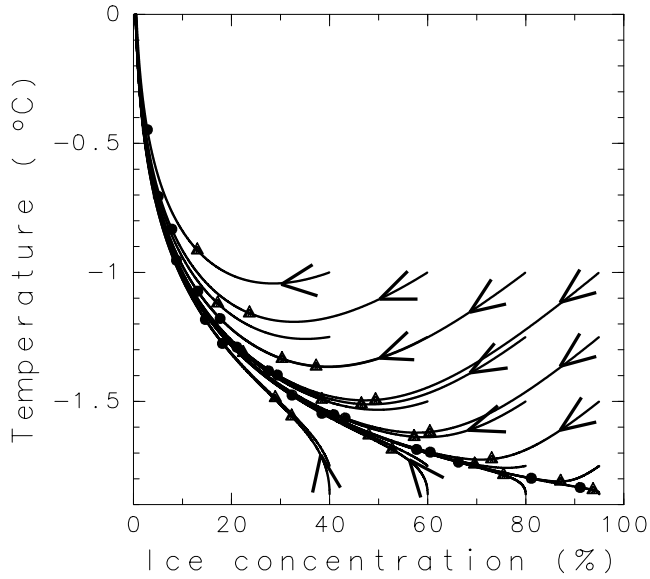

Figure 8. Time evolution of the relationship between ice concentration (C) and upper ocean temperature (T) derived from the ice–upper ocean coupled model. Trajectories of T as function of C are shown by the solid curves, with the arrows indicating the direction of time evolution. Triangles and dots designate 5 and 10 days after the integration, respectively. Cases with several initial conditions are shown, where the initial ice concentrations are set to every 20% between 40% and 95%, and the initial water temperatures are set to every 0.25°C between −1°C and −1.86°C. The thickness of the upper ocean (H), average ice thickness (h_0), net heat input at the water surface (F_n), and the bulk heat transfer coefficient between ice and ocean (K_b) are set to 25 m, 0.65 m, 160 W m^{-2}, and 1.2×10^{-4} m s^{-1}, respectively.

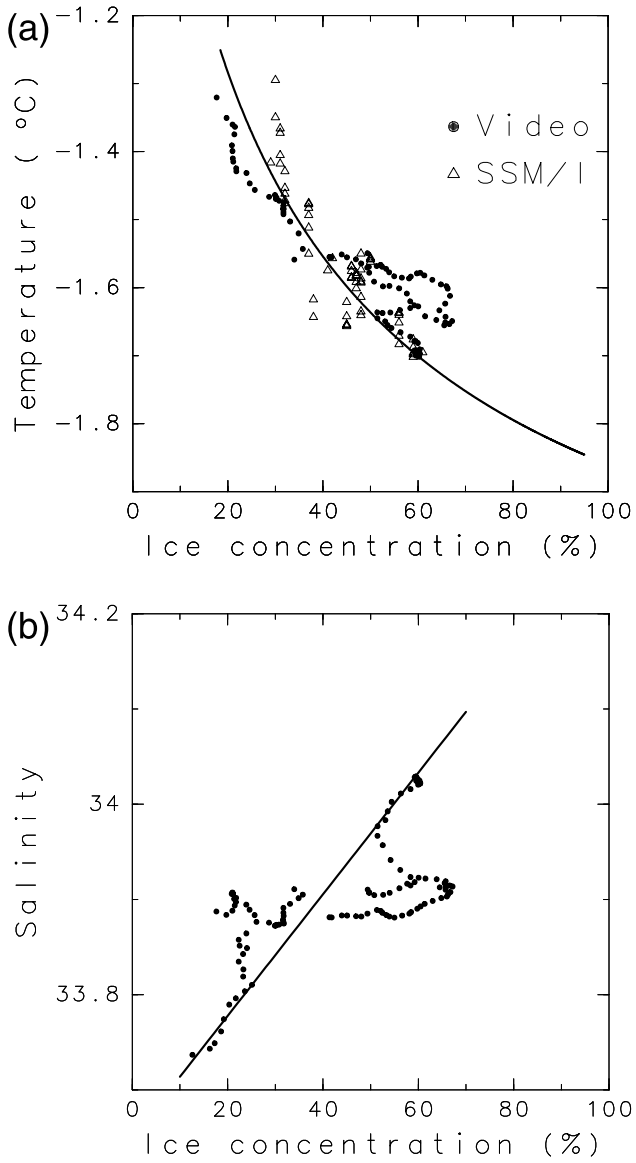

Figure 9. (a) Convergent curve with $K_b = 1.2 \times 10^{-4}$ m s^{-1} for region 1A, derived from the ice–upper ocean coupled model. For comparison, the observed CT-plot for region 1A (Figure 6a) is superimposed, where dots are from the video measurement and triangles are from the SSM/I. For the case of the CT-plot in which SSM/I data are used, the temperature data are spatially averaged using a 25-km running mean. (b) The salinity change line for region 1A, derived from the local balance of salinity in the ice–upper ocean system, superimposed on the observed CS-plot (Figure 6d).

CTD stations, ice concentration derived from SSM/I is used. The heat content of the mixed layer (Q_u) increases as ice concentration decreases, as in the case of the CT-plot for regions 1A and 1B (Figures 6a and 6b). In Figure 11, we also indicate the temperature scale corresponding to the heat content, assuming uniform temperature and constant mixed layer thickness (H = 25 m). For comparison, the convergent curve on the CT-plot obtained from the ice–upper ocean coupled model with input parameters for region 1A (Figure 9a) is superimposed, assuming that the temperature scale is correct. The convergent curve with the same K_b(= 1.2 × 10^{-4} m s^{-1}) as the CT-plot fits roughly into the obtained CQ-plot. These results support the analysis using the water temperature recorded by the underway sampling system at a depth of ~7 m.

4.2. Relationship Between Ice Concentration and Salinity

[26] Figures 6d, 6e, and 6f show ice concentration–salinity plots (hereinafter CS-plot) for regions 1A, 1B, and 2A, respectively. In the ice interior region (1A), salinity decreases as ice concentration decreases (Figure 6d), as observed in the ice interior region off Syowa Station [*Ohshima et al.*, 1998]. This relationship can be explained by the local balances of heat and salinity as follows: As ice concentration decreases, the water temperature increases because of the larger absorption of solar radiation through open water (Figure 6a), promoting ice melting and consequently a decrease in the surface salinity. At the ice margin of the Ross Sea polynya (1B), salinity decreases as ice concentration increases (Figure 6e), as observed in the ice margin region of the coastal polynya area off Syowa Station. This can be explained as follows: When sea-ice is advected into an ice-free area that has already been heated by solar radiation, the more ice is advected, the more the ice melts, leading to a decrease in salinity and then a decrease in water temperature due to the release of latent heat (Figure 6b). In region 2A, the ice interior region, a clear characteristic relationship cannot be identified (Figure 6f) probably because of the small change in salinity over a broad area.

[27] Here the local balance of salinity in the ice–upper ocean coupled system in region 1A is examined with a model similar to that of the heat balance (Figure 7). In a certain water column, if the supply of fresh water associated

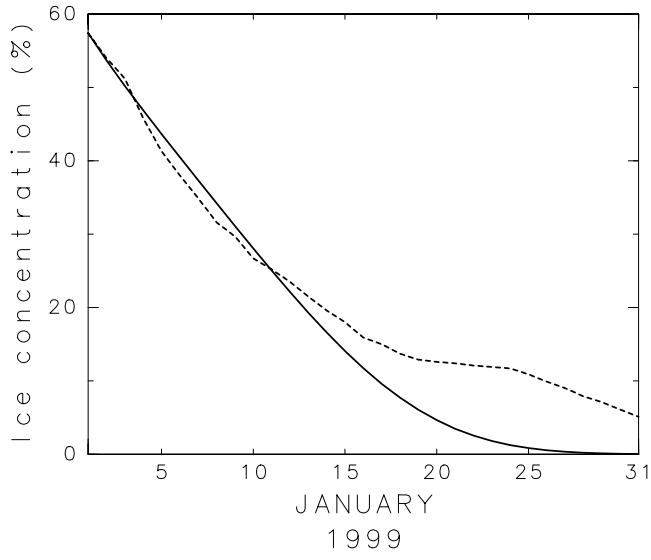

Figure 10. Time evolution of ice concentration for region 1A in January 1999 calculated from the ice–upper ocean coupled model (solid line). For comparison, the time evolution of ice concentration derived from the SSM/I is superimposed (dotted line). The observed data have been smoothed using a 7-day running mean.

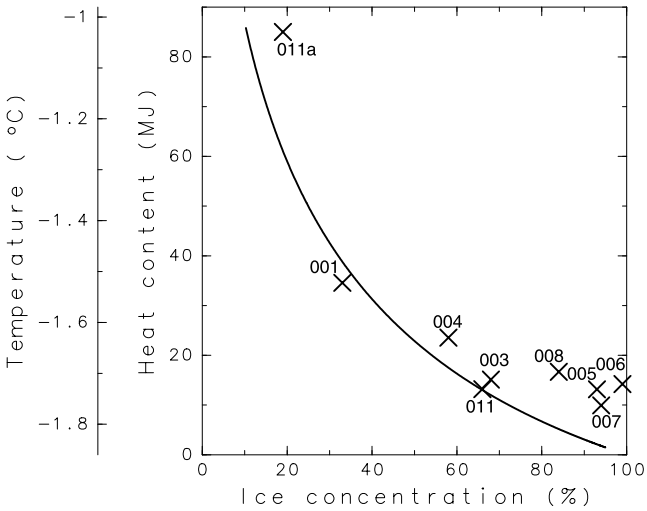

Figure 11. Scatterplot of ice concentration derived from the SSM/I versus heat content of the mixed layer for Leg 1. The heat content (Figure 4e) is estimated from each CTD data set. The numbers by the cross symbols indicate the CTD stations (Figure 1). The data at Stations 009 and 010 are not shown because the surface mixed layer cannot be identified. A temperature scale corresponding to the heat content, assuming uniform temperature and constant mixed layer thickness (H = 25 m), is also indicated. For comparison, the convergent curve on the CT-plot obtained from the ice–upper ocean coupled model with input parameters for region 1A (Figure 9a) is superimposed, assuming that the temperature scale is correct.

with sea-ice melt (ΔC) is locally used for salinity change in the upper ocean ($\Delta S = S_0 - S_1$; salinity changes from S_0 to S_1), salinity conservation is given by

$$S_1 = \frac{\rho_w H S_0 + \rho_i h_0 \Delta C S_i}{\rho_w H + \rho_i h_0 \Delta C}, \tag{4}$$

where S_i is the salinity of sea ice and is set to 6 psu from in situ observation. In an analysis area, if ice concentration and salinity at the beginning of the melt season are horizontally uniform, equation (4) implies that the CS-plot for the analysis area should be on a line with the following slope,

$$\frac{\Delta S}{\Delta C} \approx \frac{\rho_i}{\rho_w} \frac{S_w - S_i}{H} h_0. \tag{5}$$

Since ice concentration in region 1A is 94–100% at the beginning of the melt season (1 October 1998, from SSM/I data), the assumption of nearly uniform initial ice concentration in the analysis area is reasonable. The assumption that the initial salinity in the analysis area (S_0) is horizontally uniform will be described later. H and h_0 are set to 25 m and 0.65 m, respectively, as in the case of Figure 9a. The solid line in Figure 9b shows the salinity change line predicted by equation (5) superimposed on the observed CS-plot for region 1A (Figure 6d). The slope of the line roughly corresponds to that of the observed CS-plot, suggesting that the local balance of salinity nearly holds.

[28] In the above discussion we assume that initial salinity of the upper ocean in the analysis area (S_0) is horizontally uniform. From the CTD profiles (Figure 3), a remnant of the winter mixed layer with a temperature near the freezing point can be identified beneath the surface mixed layer. It is reasonable to assume that the salinity of the water near the freezing point is the initial salinity of the upper ocean (S_0). Estimated S_0 for region 1A is ~34.3 psu and ranging within ±0.1 psu. This confirms the assumption that S_0 in the analysis area is horizontally uniform.

[29] For a more quantitative discussion, we compare ice concentration with the salt deficit in the mixed layer associated with sea-ice melt ($\Delta S = S_0 - S_1$) along Leg 1, including regions 1A and 1B. S_0 and S_1 are estimated from each CTD data set. This comparison does not require the assumptions that the thickness of the mixed layer (H) and initial salinity (S_0) in the analysis area are horizontally uniform. S_1 is assumed to be the average salinity in the mixed layer when the observation was made, and is given by

$$S_1 = \frac{1}{H} \int_{z=-H}^{z=0} S(z) dz, \tag{6}$$

where $S(z)$ is the salinity observed by the CTD at a depth z, and H is the estimated thickness of the mixed layer (Figure 4e). Figure 12 shows the ice concentration–salt deficit plot (hereinafter CΔS-plot) for Leg 1. Since video measurements were not made at the CTD stations, ice concentration derived from the SSM/I is used. The estimated ΔS decreases as ice concentration decreases as in the case of the CS-plot for region 1A (Figure 6d), except at the ice margin of the Ross Sea polynya (Station 011a). For

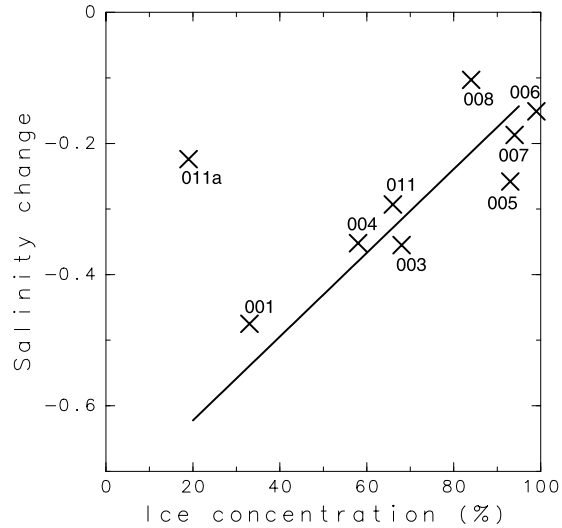

Figure 12. Scatterplot of ice concentration derived from the SSM/I versus salt deficit in the mixed layer for Leg 1. The salt deficit associated with sea-ice melt is estimated from each CTD data set. The numbers by the cross symbols indicate the CTD stations (Figure 1). The data at Stations 009 and 010 are not shown because the surface mixed layer cannot be identified. For comparison, the salinity change line for region 1A predicted by the local balance of salinity (Figure 9b) is superimposed.

Table 2. Mean Difference With Its Standard Deviation and Correlation Coefficient Among Ice Concentration Data Derived From the Video Monitoring System, Visual Observation, and SSM/I

	SSM/I Versus Video		SSM/I Versus Visual		Visual Versus Video	
Region	Mean Difference, %	Correlation Coefficient	Mean Difference, %	Correlation Coefficient	Mean Difference, %	Correlation Coefficient
Leg 1	33.4 ± 26.4	0.21	9.7 ± 19.6	0.63	23.6 ± 18.6	0.54
Leg 2	30.0 ± 21.0	0.43	11.6 ± 21.5	0.43	18.9 ± 12.6	0.80
1A	9.0 ± 14.9	0.61	−1.8 ± 15.6	0.62	10.8 ± 11.6	0.69
1B	31.7 ± 26.4	0.05	11.6 ± 29.0	0.24	19.5 ± 14.6	0.85
2A	15.3 ± 13.1	0.51	−8.6 ± 10.6	0.76	24.0 ± 8.2	0.67

comparison, the salinity change line for region 1A predicted by the local balance of salinity (the same as in Figure 9b) is superimposed. The slope of the line corresponds well to that of the CΔS-plot. This is further evidence that the local balances of salinity in the ice–upper ocean system nearly hold.

5. Summary

[30] In January 1999, ship-based observations of the sea-ice cover and upper ocean were made aboard the R/V *Nathaniel B. Palmer* in the Ross Sea, Antarctica. Various parameters of the sea-ice cover such as ice concentration, floe size, and thickness were recorded by hourly visual observation. Ice concentration was measured continuously with a video monitoring system. Water temperature and salinity at a depth of ~7 m were continuously monitored by the underway sampling system. CTD observations were made at ~1° latitude intervals. Using these various in situ data together with ice concentration data from SSM/I, sea-ice melting processes are inferred from ice–upper ocean relationships.

[31] From the comparison among ice concentration data derived from the video monitoring system, visual observation, and SSM/I, ice concentration from the video system is 20–30% smaller than those from the other methods, while the difference between the SSM/I and the visual observation is ~10% (Appendix B; Table 2). This discrepancy is particularly large in the large ice floe area (Figures 4b, 4c, 5b, and 5c). In the large ice floe area, because a ship tends to look for open water, ice concentration from the video system may be biased toward a lower value due to the relatively narrow viewing range of ~100 m.

[32] Relationships between the ice concentration derived from the video system and the temperature and salinity at a depth of ~7 m are examined in the area where the video data are expected to be reliable based on a comparison of data derived from visual observation and SSM/I. In the ice interior region, by using spatially (30 km) averaged continuous data, an ice concentration–temperature plot (CT-plot) shows that the temperature increases as ice concentration decreases (Figure 6a). A CT-plot using ice concentration from the SSM/I with wider viewing range shows similar features (Figure 9a). The CT-plot can be explained by a simple ice–upper ocean coupled model in which sea-ice melting is caused only by heat input through open water with observed input parameters of the ice thickness and mixed layer thickness (Figure 9a). The bulk heat transfer coefficient between ice and ocean (K_b) is estimated to be 1.2×10^{-4} m s^{-1} from the comparison of the observed CT-plot and the model. These are supported by an analysis of heat content in the mixed layer estimated from CTD data because the ice concentration–heat content plot is similar to the CT-plot and is explained by the model with the same K_b (Figure 11).

[33] The salinity data analyses also support the conclusion that ice melting is mainly caused by atmospheric heat input through open water. An ice concentration–salinity plot shows that the salinity at a depth of ~7 m decreases as ice concentration decreases, and is on the salinity change line predicted by the local balance of salinity in the ice–upper ocean system (Figure 9b). The salt deficit in the mixed layer associated with sea-ice melt estimated from CTD data corresponds to the salinity change predicted by the local balance (Figure 12). This also suggests that the local balance of salinity in the ice–upper ocean system nearly holds.

[34] The time evolution of ice concentration calculated from the same ice–upper ocean coupled model with the estimated K_b roughly corresponds to that derived from the SSM/I (Figure 10). Both the CT-plot and the time evolution of ice concentration are approximately explained by the same model with the same K_b. This confirms the applicability of the model and the value of K_b.

Appendix A: Comparison of Two Ice Concentration Algorithms

[35] In this study we use the enhanced NASA Team (NT2) algorithm for calculation of ice concentration from SSM/I. This algorithm is an enhancement of the NASA Team (NT) algorithm [*Cavalieri et al.*, 1984] for improving ice concentration in the Antarctic Ocean. In the summer Antarctic Ocean, the difference in ice concentration between the NT algorithm and the Bootstrap (BS) algorithm is small [*Comiso et al.*, 1997], probably because there is little new ice and surface melting. We compared ice concentration calculated using the NT2 and BS algorithms to assess whether our analysis would be affected. The average difference of ice concentration between the NT2 and BS algorithms along Leg 1 is 6.0% with standard deviation of 7.1% and correlation coefficient of 0.96. Along Leg 2, the difference and correlation coefficient are 7.8 ± 6.7% and 0.95, respectively. A CT-plot for region 1A using the BS data is quite similar to that using the NT2 data and fits the convergent curve obtained from the ice–upper ocean model with the same K_b(= 1.2×10^{-4} m s^{-1}; not shown here).

Appendix B: Comparison Among Ice Concentration Data

[36] Figures 4b and 5b show the ice concentration data derived from the video monitoring system, visual observa-

tion, and SSM/I. The video system can observe ice concentration continuously with high resolution of ~4 m in typical pack ice, although the viewing range is limited (~100 m). In the visual observation method, the spatial observation range from the ship is normally ~1 km. The hourly observation corresponds to a resolution of ~15 km in typical pack ice. The visual observation depends on the subjective judgment of each person. Here a 25-km running mean is used for the video and visual data in order to compare these data with the SSM/I data, which have a large footprint (viewing range) of ~25 km. SSM/I data for the grid point nearest the video observation site are used.

[37] Table 2 summarizes the average differences and correlation coefficients among the ice concentration data. Along Leg 1, ice concentration derived from the video system is much smaller than that from the other methods. From Figure 4b and Table 2, ice concentration data derived from the three different methods agree approximately with each other for region 1A corresponding to the segment from 0 km to 400 km. From Figure 4b, ice concentration derived from the video system is smaller than that from the SSM/I for the segment from 500 km to 1300 km. In this segment, ice concentration derived from the visual observations is also smaller than that from the SSM/I, although the difference is relatively small. These discrepancies may be caused by the different viewing ranges of the three methods. In areas with large ice floes, because a ship tends to look for open water, ice concentration from the video (and visual) observation may be biased toward a lower value due to the relatively narrow viewing range of ~100 m (and ~1 km). On the other hand, in an area with small ice floes, a ship can take a more direct line and thus the bias is small. The area where the video observation underestimates ice concentration corresponds to an area with large ice floes (typically $\geq$500 m), while the area where ice concentration data derived from the three methods agree with each other corresponds to an area with small ice floes (<100 m; Figures 4b and 4c). Along Leg 2, agreement among the three measurements is good in the small floe size area (0–500 km), while the video (and visual) measurement tends to underestimate ice concentration in the large floe size area (500–1200 km; Figures 5b and 5c).

[38] **Acknowledgments.** We thank Captain Joe Borkowski III, the officers and crew of the R/V *Nathaniel B. Palmer*, and personnel of the Antarctic Support Associates (ASA) for their support and assistance. Hideki Suetake helped with the data processing of the video monitoring system. We thank Donald J. Cavalieri for his comments and suggestion on an early version of the manuscript, and Thorsten Markus for providing the enhanced NASA Team (NT2) algorithm. Thanks are extended to Masaaki Wakatsuchi and Yasushi Fukamachi for their encouragement. Suggestions and comments from anonymous reviewers were very helpful. The DMSP-F13 SSM/I data were obtained from the EOS DAAC at the NSIDC, University of Colorado. S. N. was funded by the National Research Council through a Research Associateship Award at NASA Goddard Space Flight Center. K. O. was supported by Grant-in-Aid for Scientific Research (12640414) and RR2002 of the MEXT of the Japanese Government. M. O. J.'s involvement was made possible by National Science Foundation grant OPP-9614844.

References

Ackley, S. F., C. A. Geiger, J. C. King, E. C. Hunke, and J. Comiso (2001), The Ronne polynya of 1997–1998: Observations of air-ice-ocean interaction, *Ann. Glaciol.*, *33*, 425–429.

Cavalieri, D. J., P. Gloersen, and W. J. Campbell (1984), Determination of sea ice parameters with the Nimbus 7 SMMR, *J. Geophys. Res.*, *89*, 5355–5369.

Comiso, J. C. (1995), SSM/I ice concentrations using the Bootstrap algorithm, *NASA Ref. Publ.*, *1380*, 40 pp.

Comiso, J. C., D. J. Cavalieri, C. L. Parkinson, and P. Gloersen (1997), Passive microwave algorithms for sea ice concentration: A comparison of two techniques, *Remote Sens. Environ.*, *60*, 357–384.

Fichefet, T., and H. Goosse (1999), A numerical investigation of the spring Ross Sea polynya, *Geophys. Res. Lett.*, *26*, 1015–1018.

Gloersen, P., W. J. Campbell, D. J. Cavalieri, J. C. Comiso, C. L. Parkinson, and H. J. Zwally (1992), Arctic and Antartic sea ice, 1978–1987: Satellite passive microwave observations and analysis, *NASA SP-511*, Sci. and Tech. Inf. Program, NASA, Washington, D.C.

Hunke, E. C., and S. F. Ackley (2001), A numerical investigation of the 1997–1998 Ronne Polynya, *J. Geophys. Res.*, *106*, 22,373–22,382.

Jacobs, S. S., and J. C. Comiso (1989), Sea ice and oceanic processes on the Ross Sea continental shelf, *J. Geophys. Res.*, *94*, 18,195–18,211.

Jeffries, M. O., R. A. Shaw, K. Morris, A. L. Veazey, and H. R. Krouse (1994), Crystal structure, stable isotopes ($\delta^{18}O$) and development of sea ice in the Ross, Amundsen, and Bellingshausen seas, Antarctica, *J. Geophys. Res.*, *99*, 985–995.

Kawamura, T., M. O. Jeffries, J.-L. Tison, and H. R. Krouse (2005), Superimposed ice formation in summer on Ross Sea pack ice floes, Antarctica, *Ann. Glaciol.*, in press.

König-Langlo, G., and E. Augstein (1994), Parameterization of the downward longwave radiation at the Earth's surface in polar regions, *Meteorol. Z.*, *3*, 343–347.

Launiainen, J., and T. Vihma (1994), On the surface fluxes in the Weddell Sea, in *The Polar Oceans and Their Role in Shaping the Global Environment*, *Geophys. Monogr. Ser.*, vol. 85, edited by O. M. Johannessen et al., pp. 399–419, AGU, Washington, D. C.

Markus, T., and D. J. Cavalieri (2000), An enhancement of the NASA team sea ice algorithm, *IEEE Trans. Geosci. Remote Sens.*, *38*, 1387–1398.

Maykut, G. A., and M. G. McPhee (1995), Solar heating of the Arctic mixed layer, *J. Geophys. Res.*, *100*, 24,691–24,703.

Maykut, G. A., and D. K. Perovich (1987), The role of shortwave radiation in the summer decay of a sea ice cover, *J. Geophys. Res.*, *92*, 7032–7044.

McPhee, M. G. (1992), Turbulent heat flux in the upper ocean under sea ice, *J. Geophys. Res.*, *97*, 5365–5379.

McPhee, M. G., and D. G. Martinson (1994), Turbulent mixing under drifting pack ice in the Weddell Sea, *Science*, *263*, 218–221.

Morris, K., and M. O. Jeffries (2001), Seasonal contrasts in snow cover characteristics on Ross Sea ice floes, *Ann. Glaciol.*, *33*, 61–68.

Nihashi, S., and K. I. Ohshima (2001), Relationship between the sea ice decay and solar heating through open water in the Antarctic sea ice zone, *J. Geophys. Res.*, *106*, 16,767–16,782.

Ohshima, K. I., and S. Nihashi (2005), A simplified ice-ocean coupled model for the Antarctic ice melt season, *J. Phys. Oceanogr.*, in press.

Ohshima, K. I., K. Yoshida, H. Shimoda, M. Wakatsuchi, T. Endoh, and M. Fukuchi (1998), Relationship between the upper ocean and sea ice during the Antarctic melting season, *J. Geophys. Res.*, *103*, 7601–7615.

Parkinson, C. L., and W. M. Washington (1979), A large-scale numerical model of sea ice, *J. Geophys. Res.*, *84*, 311–337.

Worby, A. P., and I. Allison (1999), A technique for making ship-based observation of Antarctic sea ice thickness and characteristics: I. Observational techniques and results, *Res. Rep. 14*, pp. 1–23, Antarct. Coop. Res. Cent., Hobart, Tasmania, Australia.

Zillman, J. W. (1972), A study of some aspects of the radiation and heat budgets of the Southern Hemisphere oceans, *Meteorol. Stud. 26*, 562 pp., Bur. of Meteorol., Dep. of the Inter., Canberra, ACT, Australia.

M. O. Jeffries, Geophysical Institute, University of Alaska Fairbanks, 903 Koyukuk Drive, P. O. Box 757320, Fairbanks, AK 99775-7320, USA.

T. Kawamura, S. Nihashi, and K. I. Ohshima, Institute of Low Temperature Science, Hokkaido University, Sapporo 060-0819, Japan. (sohey@lowtem.hokudai.ac.jp)